



**HAL**  
open science

## Impact flash evolution of CO<sub>2</sub> ice, water ice, and frozen Martian and lunar regolith simulant targets

Jon Tandy, Mark C. Price, Penny Wozniakiewicz, Mike Cole, Luke Alesbrook,  
Chrysa Avdellidou

### ► To cite this version:

Jon Tandy, Mark C. Price, Penny Wozniakiewicz, Mike Cole, Luke Alesbrook, et al.. Impact flash evolution of CO<sub>2</sub> ice, water ice, and frozen Martian and lunar regolith simulant targets. *Meteoritics and Planetary Science*, 2020, 10.1111/maps.13581 . hal-03038649

**HAL Id: hal-03038649**


**<https://hal.science/hal-03038649>**

Submitted on 3 Dec 2020

**HAL** is a multi-disciplinary open access archive for the deposit and dissemination of scientific research documents, whether they are published or not. The documents may come from teaching and research institutions in France or abroad, or from public or private research centers.

L'archive ouverte pluridisciplinaire **HAL**, est destinée au dépôt et à la diffusion de documents scientifiques de niveau recherche, publiés ou non, émanant des établissements d'enseignement et de recherche français ou étrangers, des laboratoires publics ou privés.

## Impact flash evolution of CO<sub>2</sub> ice, water ice, and frozen Martian and lunar regolith simulant targets

Jon D. TANDY \*, Mark C. PRICE<sup>2</sup>, Penny J. WOZNAKIEWICZ<sup>2</sup>, Mike J. COLE<sup>2</sup>,  
Luke S. ALESBROOK<sup>2</sup>, and Chrysa AVDELLIDOU<sup>3</sup>

<sup>1</sup>School of Human Sciences, London Metropolitan University, London N7 8DB, UK

<sup>2</sup>Centre for Astrophysics and Planetary Science, School of Physical Sciences, Ingram Building, University of Kent,  
Canterbury CT2 7NH, UK

<sup>3</sup>Laboratoire Lagrange, Boulevard de l'Observatoire, CS 34229, Nice 06304, France

\*Corresponding author. E-mail: j.tandy@londonmet.ac.uk

(Received 06 November 2019; revision accepted 11 September 2020)

---

**Abstract**—The wavelength dependence and temporal evolution of the hypervelocity impact self-luminous plume (or “flash”) from CO<sub>2</sub> ice, water ice, and frozen Martian and lunar regolith simulant targets have been investigated using the Kent two-stage light-gas gun. An array of 10 band-pass filtered photodiodes and a digital camera monitored changes in the impact flash intensity during the different phases of the emitting ejecta. Early-time emission spectra were also recorded to examine short-lived chemical species within the ejecta. Analyses of the impact flash from the varied frozen targets show considerable differences in temporal behavior, with a strong wavelength dependence observed within monitored near-UV to near-IR spectral regions. Emission spectra showed molecular bands across the full spectral range observed, primarily due to AlO from the projectile, and with little or no contribution from vaporized metal oxides originating from frozen regolith simulant targets. Additional features within the impact flash decay profiles and emission spectra indicate an inhomogeneity in the impact ejecta composition. A strong correlation between the density of water ice-containing targets and the impact flash rate of decay was shown for profiles uninfluenced by significant atomic/molecular emission, although the applicability to other target materials is currently unknown. Changes in impact speed resulted in considerable differences in the temporal evolution of the impact flash, with additional variations observed between recorded spectral regions. A strong correlation between the impact speed and the emission decay rate was also shown for CO<sub>2</sub> ice targets. These results may have important implications for future analyses of impact flashes both on the lunar/Martian surface and on other frozen bodies within the solar system.

---

### INTRODUCTION

Intense, short-lived light flashes are produced during hypervelocity impacts; indeed, flashes resulting from high-speed lunar impacts are so energetic that they are frequently observed by modest facilities (Dunham et al. 2000; Cudnik et al. 2003; Suggs et al. 2014; Avdellidou and Vaubaillon 2019). In order to understand the complex phenomena within such impact ejecta, laboratory measurements are utilized to more closely observe these impacts and identify the

multiple, interacting processes within the rapidly evolving ejecta.

The temporal evolution of impact flashes is typically monitored in the laboratory using photodetectors (Eichhorn 1976; Burchell et al. 1996; Ernst and Schultz 2003, 2004, 2007; Bergeron et al. 2006; Lawrence et al. 2006; Tsembelis et al. 2008; Ernst et al. 2011; Goel et al. 2015; Yafei et al. 2019) or high-speed cameras (Kondo and Ahrens 1983; Schultz 1996; Ernst and Schultz 2007; Schultz et al. 2007; Mihaly et al. 2013, 2015; Tandy et al. 2014; Schultz and Eberhardy 2015), revealing

multiple phases of the radiating impact ejecta. These phases primarily comprise a rapid jet or plasma phase; a slower, expanding vapor cloud; and molten or high temperature ejecta that are dependent on specific impact parameters (Ang 1990; Yang et al. 1992; Kadono and Fujiwara 1996; Schultz 1996; Sugita et al. 1998; Sugita and Schultz 1999; Ernst and Schultz 2004, 2007; Schultz et al. 2006; Tsembelis et al. 2008; Ernst et al. 2011; Bruck Syal et al. 2012). Several studies have also utilized spectroscopic instrumentation to further analyze the composition of the rapidly evolving ejecta plume, allowing determination of prevalent atomic and/or molecular species (Gehring and Warnica 1963; Jean and Rollins 1970; Schultz et al. 1996, 2007; Sugita et al. 1998, 2003; Sugita and Schultz 1999, 2003a; Lawrence et al. 2006; Tandy et al. 2014; Schultz and Eberhardy 2015; Verreault et al. 2015).

Previous impact experiments into ices have determined the importance and degree of melting, vaporization, and ionization within the ejecta (Timmermann and Grün 1991; Burchell et al. 1996; Schultz and Mustard 2004; Schultz et al. 2007; Bruck Syal et al. 2012; Rager et al. 2014). It is likely that these highly energetic impacts drastically alter the physical and chemical properties of icy bodies and could play a significant role in the evolution of planetary surface composition and the areas of space in their vicinity (Pospieszalska and Johnson 1991; Timmermann and Grün 1991; Burchell et al. 1996; Martins et al. 2013). The temporal changes in the emission and the transient chemical species generated from these frozen targets, therefore, warrant further investigation.

This study investigates the wavelength dependence and temporal evolution of hypervelocity impact flashes from CO<sub>2</sub> ice, water ice, and frozen Martian and lunar regolith simulant targets. An additional analysis of corresponding early-time emission spectra assesses contribution from specific atomic/molecular species within the initial ejecta. Variations in the observed phenomena with impact speed are also reported.

## METHOD

A two-stage light-gas gun (Burchell et al. 1999) was used to horizontally accelerate 3.0 mm 7075 aluminum spheres into various frozen targets with their surface aligned at 90° to the shot line (horizontal impact). The impact speed was selected by varying the amount of gunpowder and gas pressure in the gun's pump tube. The majority of experiments used an impact speed between 4.5 and 5.0 km s<sup>-1</sup>, with the exact speed measured to better than 1% for individual shots. The target chamber was evacuated to typically 50 mbar during each shot. This pressure is higher than typical



Fig. 1. A 100 mm diameter, stainless steel can containing a frozen ~50:50 mixture of finely crushed CO<sub>2</sub> ice and JSC-1 Martian regolith simulant.

vacuum conditions employed by some other impact flash experiments (e.g., Tandy et al. 2014; Schultz and Eberhardy 2015) and will reduce the mean free path of the ejecta. This will cause an increase in ablation of the high-speed ejecta, with a higher proportion of emission from the resulting high temperature vapor (Sugita and Schultz 2003b). Consequently, the overall nature and behavior of the observed impact flash may differ from laboratory experiments utilizing lower ambient pressures. Frozen targets containing a combination of water ice, CO<sub>2</sub> ice, and regolith simulants were prepared and compressed into 100 mm diameter, stainless steel cans, as illustrated in Fig. 1.

The chemical compositions (percentage by weight) of the JSC-1A lunar simulant (McKay et al. 1994) and JSC-1 Martian simulant (Allen et al. 1998) are summarized in Appendix A. The average grain size of the lunar and Martian regolith simulants is approximately 188 and 325 μm, respectively. Targets containing ice and regolith simulant were thoroughly mixed during preparation to ensure an even distribution of materials within the target. A fine spray of water was required to bind the regolith simulants to the finely crushed CO<sub>2</sub> ice before refreezing the mixtures (Avdellidou et al. 2017). Targets were stored at approximately -140 °C prior to impact to prevent significant CO<sub>2</sub> ice sublimation (for ~30 min on

average). Targets were then exposed to room temperature for approximately 10 min while the impact chamber was evacuated. Given an approximate sublimation rate of 2% per hour for typical dry ice pellets, this would correspond to approximately 0.33% of the sample. However, this is likely an overestimate, as the ice is compressed within a steel with only the target surface exposed to the ambient air within the vacuum chamber (i.e., a smaller surface area). Furthermore, the sublimation of the target surface is partially dependent on the heat transfer from the residual air, which decreases relatively rapidly once evacuation begins. Despite the relatively small loss due to sublimation, rapid thermal diffusion within the sample during evacuation would cause the target material excavated during impact to be at room temperature.

The approximate, average densities of targets containing water ice were determined by preparing multiple samples on a smaller scale (approximately 2.5 cm<sup>3</sup>) and measuring their volume and mass using Vernier calipers and a top pan balance, respectively. Densities of 0.92, 1.32, and 1.73 g cm<sup>-3</sup> were calculated for the 100% water ice, 50% water ice/50% JSC-1 Martian regolith, and 50% water ice/50% JSC-1A lunar regolith samples, respectively. The percentage relative standard deviation of the calculated densities was 3.4%, 4.8%, and 2.0%, respectively. Densities for targets containing CO<sub>2</sub> ice could not be acquired using this method due to rapid sublimation during measurements. It was also not possible to determine changes in densities for targets containing CO<sub>2</sub> ice during evacuation of the target chamber. Approximate densities for these materials were determined by comparing emission decay data with those from targets containing water ice during subsequent analyses (detailed later). Table 1 summarizes the target material and projectile speed used within each impact experiment.

### Impact Flash Decay Measurements

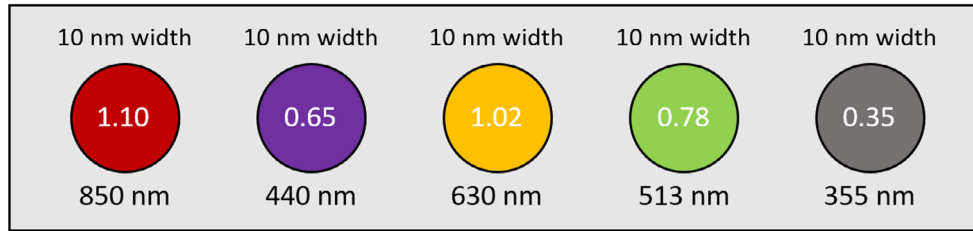
Initial experiments monitored the impact flash intensity and decay across 10 spectral bands (between 355 and 950 nm) using an array of identical photodiodes with a spectral width of approximately 300–1100 nm. The photodiodes were arranged in two banks, with different optical/IR band-pass filters and encased in a protective aluminum box. The arrangement of each photodiode within the box, including the band center, transmission efficiency, and spectral width of each filter, is indicated in Fig. 2. The broader spectral width (60 nm) of the 400 nm filter was utilized to capture the strong, aluminum atomic emission at 394

Table 1. Frozen target material and projectile speed for each impact experiment. All experiments were carried out using a horizontal impact orientation (target at 90° to the shot line).

Shot ID	Target material and percentage composition	Impact speed (km s <sup>-1</sup> )
S1	100% CO <sub>2</sub> ice	4.77
S2	100% water ice	4.51
S3	50% CO <sub>2</sub> ice/50% JSC-1 Martian regolith simulant	4.61
S4	50% water ice/50% JSC-1 Martian regolith simulant	4.66
S5	50% CO <sub>2</sub> ice/50% JSC-1A lunar regolith simulant	4.73
S6	50% water ice/ 50% JSC-1A lunar regolith simulant	4.31
S7	100% CO <sub>2</sub> ice	4.92
S8	100% CO <sub>2</sub> ice	5.01
S9	100% CO <sub>2</sub> ice	4.84
S10	50% CO <sub>2</sub> ice/50% JSC-1 Martian regolith simulant	4.89
S11	50% CO <sub>2</sub> ice/50% JSC-1 Martian regolith simulant	4.91
S12	50% CO <sub>2</sub> ice/50% JSC-1 Martian regolith simulant	4.78
S13	50% CO <sub>2</sub> ice/50% JSC-1A lunar regolith simulant	4.86
S14	50% CO <sub>2</sub> ice/50% JSC-1A lunar regolith simulant	4.74
S15	50% CO <sub>2</sub> ice/50% JSC-1A lunar regolith simulant	4.81
S16	100% CO <sub>2</sub> ice	4.03
S17	100% CO <sub>2</sub> ice	4.85
S18	100% CO <sub>2</sub> ice	5.73
S19	100% CO <sub>2</sub> ice	5.50

and 396 nm. The photodiode box was placed within the target chamber and positioned slightly below the shot line and approximately 650 mm from target surface, as indicated in Fig. 3. Photodiodes were mounted approximately 5 mm apart with a field of view diameter of approximately 25 cm at the point of impact. Two small alignment lasers within the box were used to ensure the photodiodes' field of view (FOV) were directed at the center of the target before each shot. The alignment accuracy was determined to be <0.1°. This accuracy, coupled with the large photodiode FOV, ensured each channel recorded the same impact-induced emission. The output of each photodiode was connected via an electrical feedthrough to a high-speed data acquisition system. Triggering was achieved from the moment of impact of the discarded sabot segments onto a stop-plate with a polyvinylidene difluoride (PVDF) sensor attached. This resulted in approximately 100 μs

Photodiode Bank 1



Photodiode Bank 2

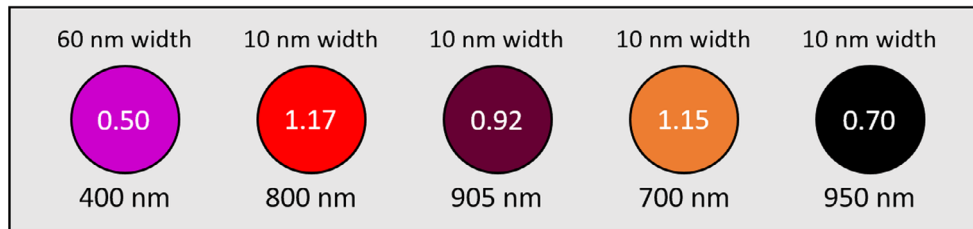


Fig. 2. Arrangement of two photodiode banks with band-pass filter spectral widths (above), transmission efficiencies (inside), and center wavelengths (below).

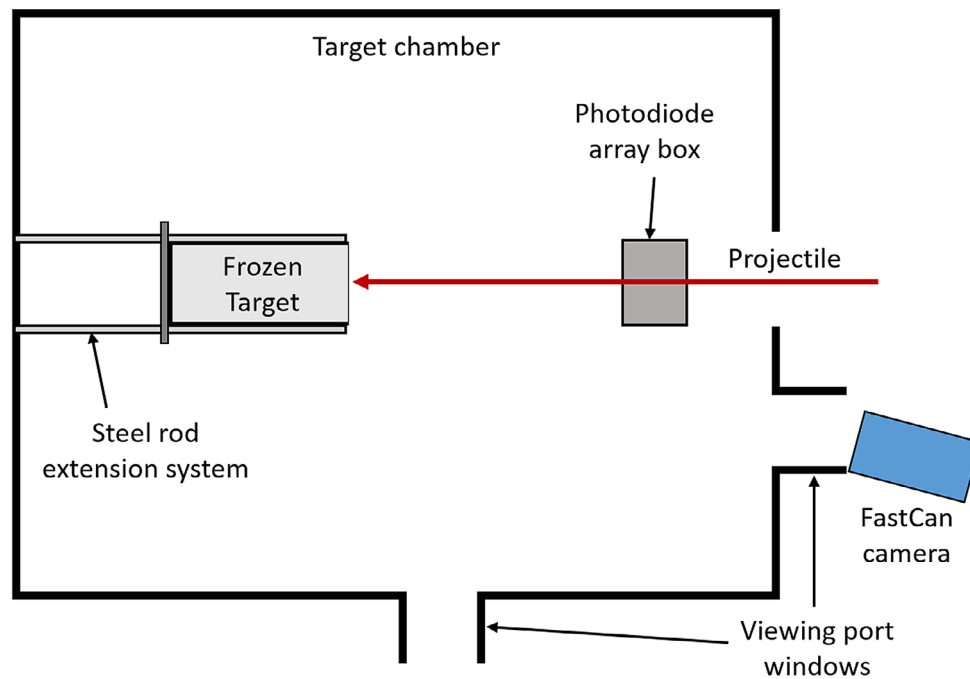


Fig. 3. Arrangement of the frozen target, photodiode array box, and FastCan camera during impact flash decay measurements (not to scale).

of pre-impact data from the photodiodes before the projectile impacted the target. The resulting emission intensity data have a time resolution of  $1.0 \mu\text{s}$ .

The impact flash intensities across different spectral bands for shots S1–S6 and S16–S19 were measured using the photodiode array. The resulting data for each spectral band was adjusted to account for the quantum efficiency

of the photodiode ( $\sim 0.5$  across all wavelengths) and normalized according to the transmission efficiency at the central wavelength of each band-pass filter (shown in Fig. 2). The inherent background voltage of each channel's baseline was then slightly raised or lowered to approximately  $10.0 \text{ mV}$  (through addition or subtraction of a specific value, independent for each channel) to allow

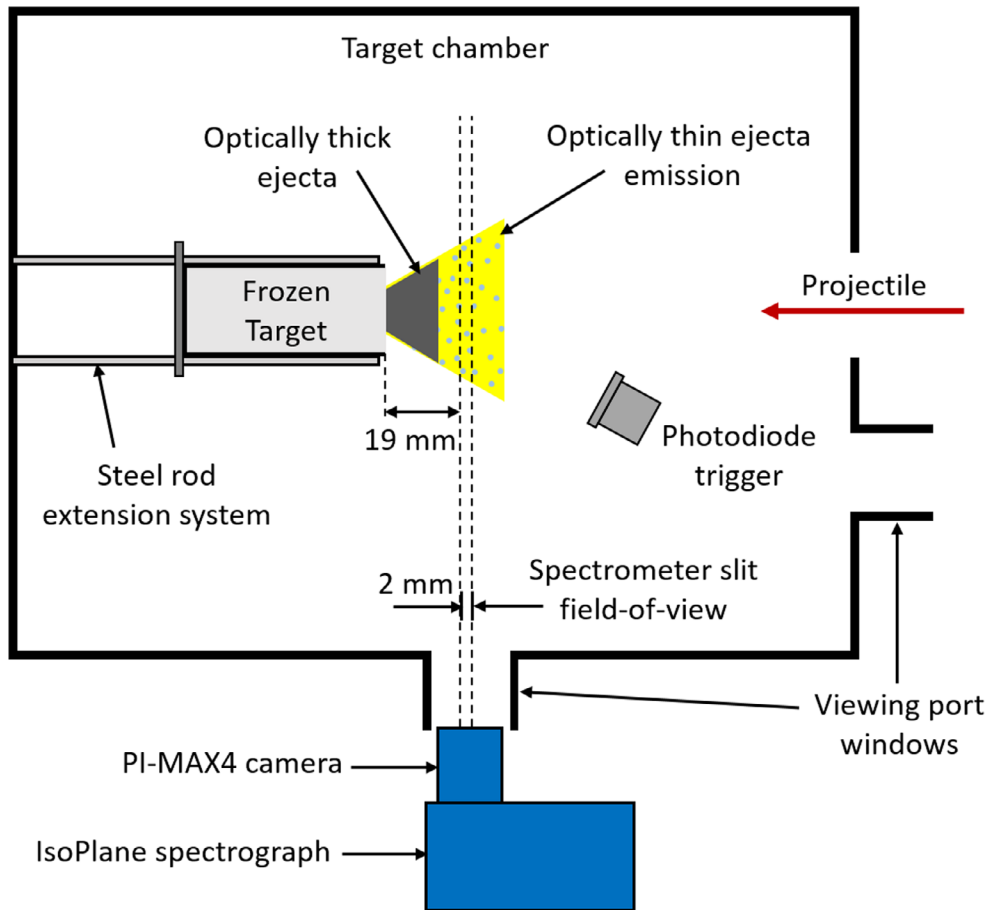


Fig. 4. Arrangement of the frozen target, IsoPlane spectrograph, PI-MAX 4 camera, and photodiode trigger during early-time emission spectra measurements (not to scale). The spectrometer slit width provided a field of view of  $2 \times 91$  mm (width  $\times$  height) positioned 19 mm in front of the frozen target surface.

a direct comparison of the relative intensities of each spectral band.

Additional photographs of the impact flash were recorded through a window in the target chamber approximately 1.1 m and  $15^\circ$  from the projectile shot line using a FastCan digital video camera (as shown in Fig. 3). The camera utilized a 50 mm Nikon f1.2 lens with a resolution of  $1024 \times 360$ . As the camera was unable to be externally triggered, it was operated continuously at a frame rate of 2800 frames/s and selected frames (showing the impact flash) extracted post-shot.

### Early-Time Emission Spectra

Optical emission spectra of the initial impact ejecta cloud (within  $\sim 15 \mu\text{s}$ ) were recorded through a side window of the impact chamber (at  $90^\circ$  to the shot line) using a Princeton Instruments ultra-fast, PI-MAX4 intensified camera and IsoPlane spectrograph (as shown in Fig. 4). A  $600 \text{ g mm}^{-1}$  diffraction grating blazed at

500 nm was utilized within the spectrometer providing a spectral width and resolution (FWHM) of approximately 60 and 0.2 nm, respectively. Consequently, data from three individual shots (using identical impact conditions) were combined to produce emission spectra covering a full spectral range of 470–640 nm. The spectral range of the three segments was 468.7–530.9, 528.9–590.8, and 584.0–645.6 nm, respectively. Small variations in the baseline intensity of each segment were adjusted by adding/subtracting a constant factor to slightly increase/decrease the overall intensity of the segment as required. The emission spectra were restricted to targets containing  $\text{CO}_2$  ice and  $\text{CO}_2$  ice/regolith mixtures, due to weak emission from the water ice targets and limited experimental time with the spectrometer system.

The PI-MAX4 camera utilized a Nikon AF-S micro Nikkor 105 mm lens focused at the center of the target chamber. The spectrometer slit width was set to  $250 \mu\text{m}$  providing a field of view of  $2 \times 91$  mm (width  $\times$  height) positioned 19 mm in front of the frozen target surface to minimize obscuration from fast-moving, solid/liquid

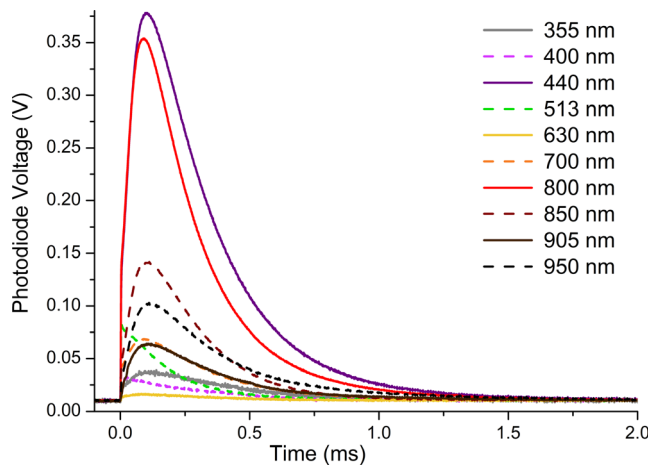


Fig. 5. Impact flash decay measurements over 10 spectral bands from a 3 mm Al projectile impacting a solid CO<sub>2</sub> ice target at 4.77 km s<sup>-1</sup>. The wavelengths shown are the central wavelengths of each band-pass filter, as indicated in Fig. 2.

ejecta during the camera exposure, as indicated in Fig. 4. The system was triggered from the initial impact flash using a photodiode placed within the target chamber, approximately 150 mm from the target (shown in Fig. 4). The camera exposure time was set to 10  $\mu$ s with the trigger delay time (response delay from the photodiode) dependent on the target. The average variation in the trigger delay for each target material was  $\pm 0.9 \mu$ s. Previous work using similar impact conditions showed that the ejecta present within the first microsecond is typically optically thick (Heunoske et al. 2013). Fortunately, the trigger delay within these experiments effectively ensured that all spectra measured optically thin ejecta and exclusively observed spectra in emission.

## RESULTS

Preliminary impact flash measurements showed reproducible temporal behavior of the individual photodiodes, allowing a comparison between channels. Figure 5 shows the impact flash decay of each photodiode over the first 2 ms for a pure CO<sub>2</sub> ice target (shot S1) indicating variation across the different spectral bands. Additionally, Fig. 6 shows three sequential FastCan camera images (exposure time approximately 0.35 ms) corresponding to frames in which the impact emission was visible during shot S1.

A subsequent examination of the impact flash in individual photodiode channels for different target materials indicated considerable variation in both the peak intensity and decay profiles of the ejecta emission. Furthermore, these variations were shown to be different for specific spectral bands. This is illustrated in

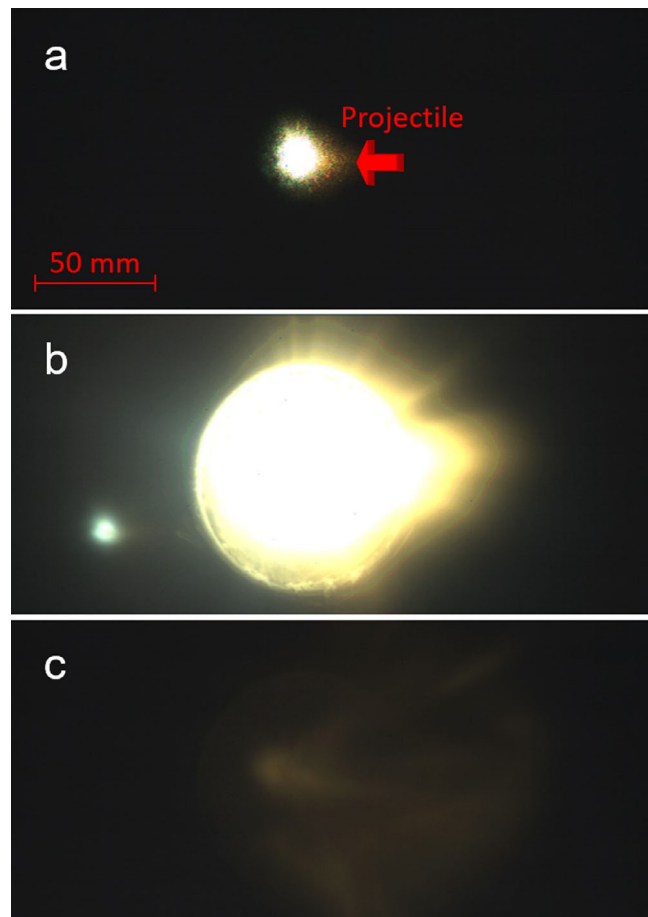


Fig. 6. Photograph sequence (a–c) of the impact flash from a 3 mm Al projectile impacting a solid CO<sub>2</sub> ice target at 4.77 km s<sup>-1</sup>. Images were acquired using a FastCan camera aligned approximately 15° from the projectile shot line, operating at 2800 frames/s, corresponding to an exposure time of  $\sim 0.35$  ms. Exact timings of each frame relative to the impact time could not be acquired due to the inability to externally trigger the camera. The bright area on the left side of image (b) is due to specular reflection from the steel can containing the frozen target. The edge of the steel can is also observed as the circular feature in image (b).

Fig. 7, which shows the variation in impact flash decay profiles of the six target materials for all photodiode channels except those with filters centered at 400 and 630 nm (note the differences in the voltage scale for each channel). The 400 nm channel was not used for this comparison due to the different spectral width of the band-pass filter (60 nm in comparison to 10 nm for all other filters). The 630 nm photodiode data were also not included due to the extremely low intensities consistently measured by this channel.

Despite variations in temporal behavior between targets, Fig. 7f shows a uniform decay profile for all materials. These data were used to calculate decay exponents ( $\alpha$ ) for each material using the method

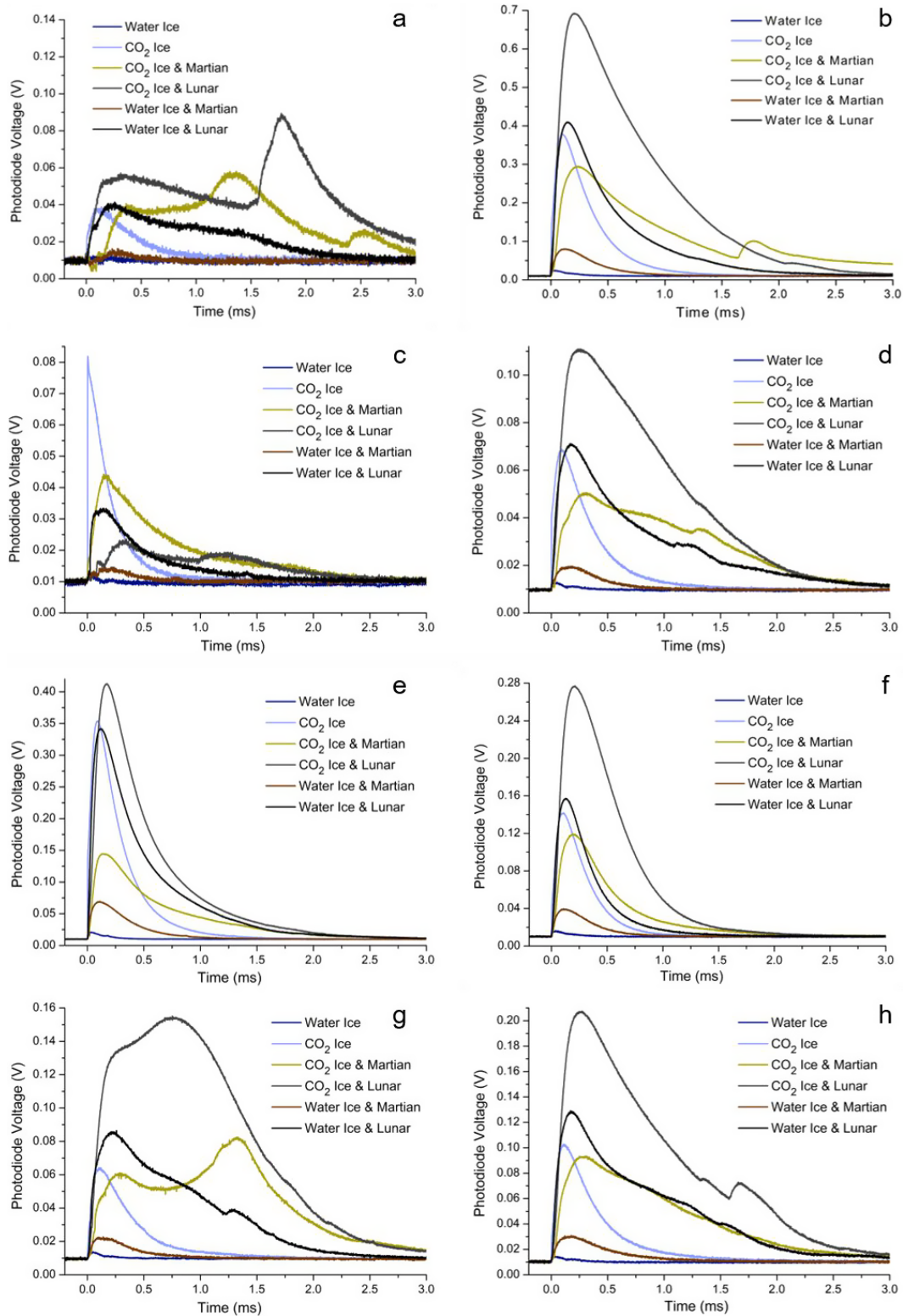


Fig. 7. Impact flash decay measurements from a 3 mm diameter Al projectile impacting six different target materials, as indicated in Table 1 (shots S1–S6). The central wavelengths of the eight spectral bands shown are (a) 355 nm, (b) 440 nm, (c) 513 nm, (d) 700 nm, (e) 800 nm, (f) 850 nm, (g) 905 nm, and (h) 950 nm, respectively.



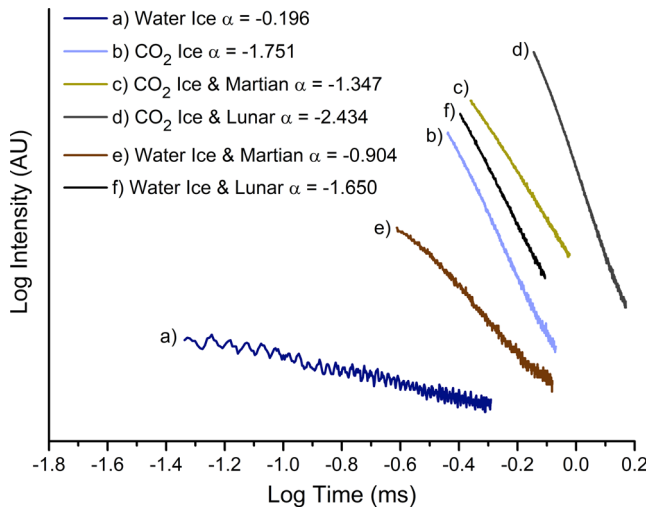


Fig. 8. Decay curves and corresponding decay exponents ( $\alpha$ ) using the 850 nm photodiode data for each frozen target.

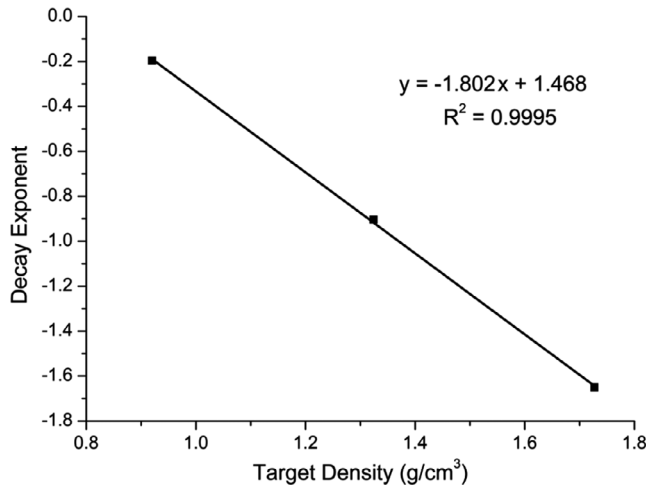


Fig. 9. Decay exponent ( $\alpha$ ) versus target density for 100% water ice, 50% water ice/50% Martian regolith simulant, and 50% water ice/ 50% lunar regolith simulant targets. The best-fit equation indicates a linear relationship.

outlined by Ernst and Schultz (2003) with the resulting decay curves shown in Fig. 8.

Decay exponents obtained for each water-containing target showed a strong correlation to the measured target densities, as shown in Fig. 9. Equivalent data points were not plotted for CO<sub>2</sub>-containing targets, as accurate density values could not be determined due to rapid sublimation during measurements.

An analysis of the variation in decay profile with impact speed was also undertaken. Figures 10, 11, and 12 compare the flash decay profiles from shots S16–S18

for the 440, 513, and 630 nm photodiode channels, respectively.

Decay exponents ( $\alpha$ ) for four CO<sub>2</sub> ice impacts at varied impact speeds (shots S16–S19) were calculated using the 850 nm photodiode channel measurements. These  $\alpha$  values showed a strong correlation to the impact speed, as shown in Fig. 13.

Early-time emission spectra were also recorded and combined (as described in the Methods section) for pure CO<sub>2</sub> ice (shots S7–S9), CO<sub>2</sub> ice and Martian regolith (shots S10–S12), and CO<sub>2</sub> ice and lunar regolith (S13–S15) targets, which are shown in Figs. 14, 15, and 16, respectively.

Further analysis of the data revealed differences in the emission spectrum in different areas of the camera CCD, corresponding to different vertical positions within the ejecta. The CO<sub>2</sub> ice impact data were subsequently binned into 15 segments (rows of CCD pixels) corresponding to a field of view of approximately 2 × 6 mm (width × height). Figure 17 indicates the different emission spectra of shot S7 for two of these segments showing the strongest emission.

## DISCUSSION

The impact flash decay observed across the different spectral channels shown in Fig. 5 indicates a variation in both the peak intensity and temporal behavior of the emission. Although normalized for photodiode quantum efficiency, it is difficult to provide a fully quantitative comparison of the peak flash intensity across the different channels, as the photodiode array was not calibrated to take into account additional variations between photodiodes (e.g., sensitivity, filter efficiency, etc.). Indeed, a precise, quantitative analysis of the peak emission across the spectral bands covered by each photodiode is beyond the scope of this article. Nevertheless, the photodiode data suggest that certain spectral regions (e.g., around 440 and 800 nm) emit more in the initial 250  $\mu$ s than others (e.g., around 400 and 630 nm).

Figure 5 also shows that, in general, the emission decay profile is similar in the majority of the photodiode channels and returns the baseline at around 1.5 ms. The figure also indicates that most channels peak between approximately 70 and 100  $\mu$ s after impact. The observed emission should be primarily due to thermal radiation from the hot, expanding gas cloud present after the initial jetting phase. The uniformity in the majority of decay profiles is consistent with a cooling blackbody within an expanding gas cloud (Ernst and Schultz 2004; Schultz and Eberhardy 2015). Figure 6 illustrates this rapid expansion and cooling of the ejecta within the sequence of impact flash photographs and indicates that

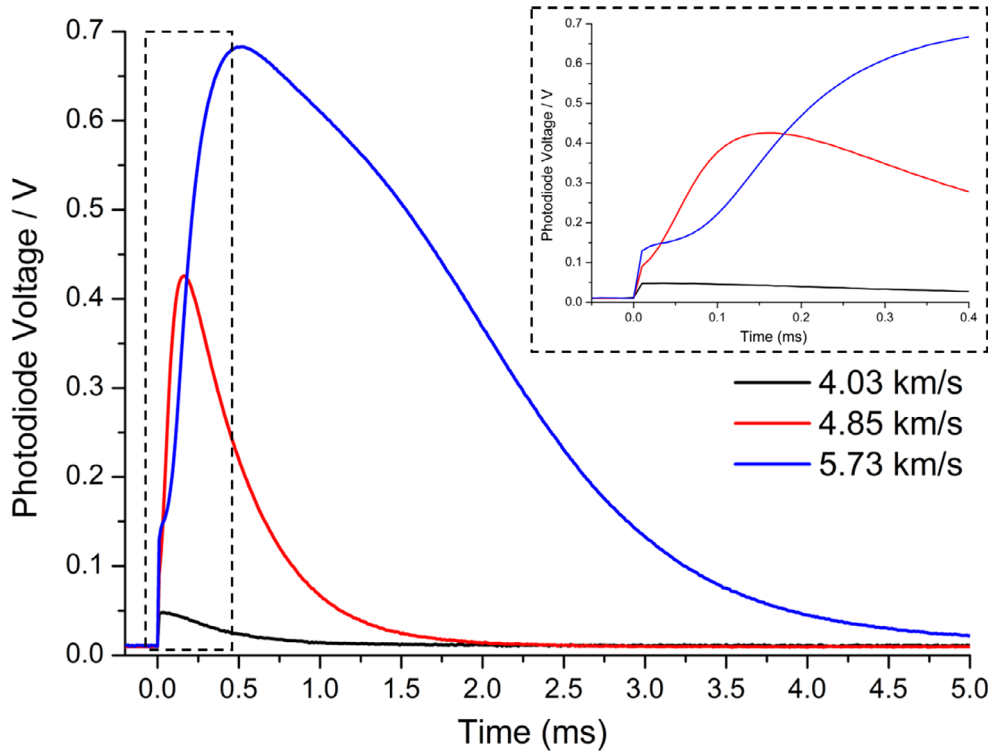


Fig. 10. Impact flash measurements of the 440 nm photodiode channel for a 3 mm diameter Al impact onto a CO<sub>2</sub> ice target at three different impact velocities. The insert in the top right of the figure shows the difference in emission profile within the first 0.4 ms.

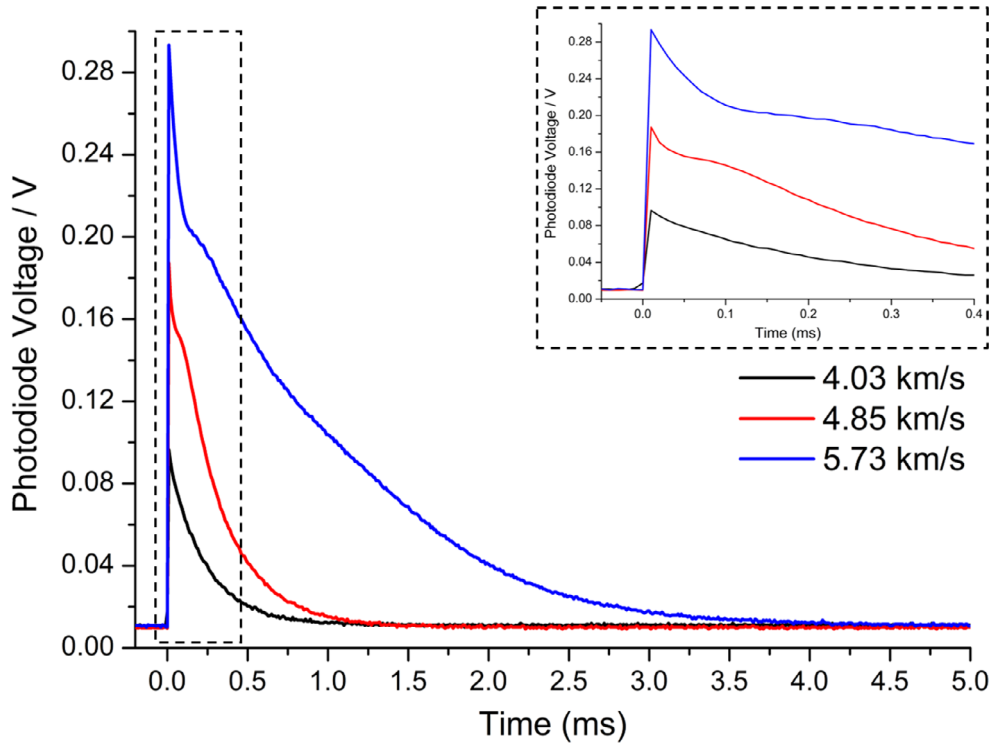


Fig. 11. Impact flash measurements of the 513 nm photodiode channel for a 3 mm diameter Al impact onto a CO<sub>2</sub> ice target at three different impact velocities. The insert in the top right of the figure shows the difference in emission profile within the first 0.4 ms.

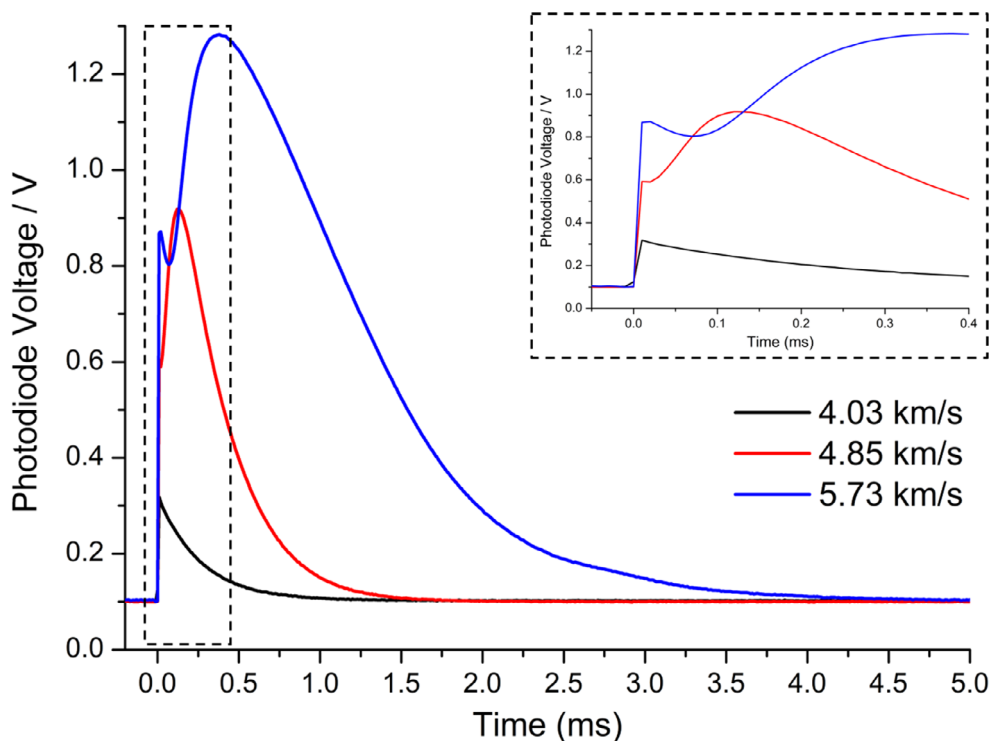


Fig. 12. Impact flash measurements of the 630 nm photodiode channel for a 3 mm diameter Al impact onto a CO<sub>2</sub> ice target at three different impact velocities. The insert in the top right of the figure shows the difference in emission profile within the first 0.4 ms.

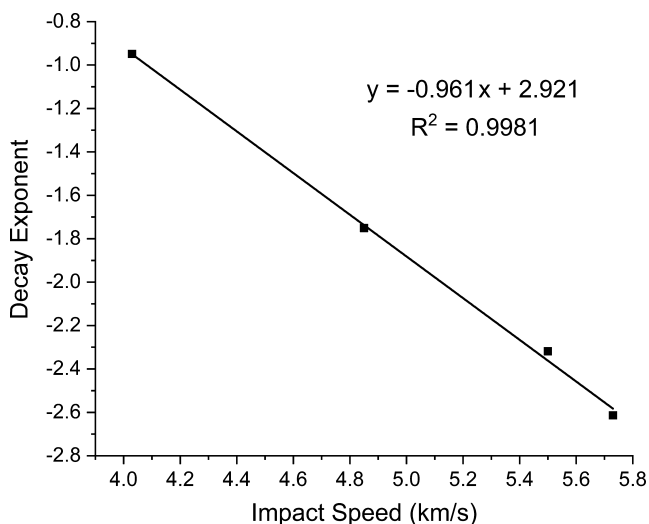


Fig. 13. Decay exponent ( $\alpha$ ) versus impact speed for 100% CO<sub>2</sub> ice targets. The best-fit equation indicates a linear relationship.

the increase in photodiode intensities to their peak is primarily due to an expansion of the radiating area exposed to the detectors.

A similar study by Ernst and Schultz (2004) examined the peak emission intensity during spherical

Pyrex impacts into pumice dust targets using six calibrated photodiodes with various band-pass filters. The resulting data showed the maximum intensities for the filtered photodiodes to be approximately the same, with no clear trend between wavelength and peak emission intensity. Conversely, Yafei et al. (2019) observed considerable variation in the peak intensities of four photodiodes monitoring different wavelengths (400, 500, 600, and 700 nm) during impacts of Al projectiles onto Al plates. This suggests that the projectile and/or target materials play a pivotal role in the relative strength of the emission across the visible and near-IR spectrum.

Figure 5 also shows inconsistencies in the integrated intensities and peak times between photodiodes. Two notable exceptions are the 400 and 513 nm channels, which peak at 25 and 4  $\mu$ s, respectively. Analyses by Ernst and Schultz (2003) of impact emission decay using photodiodes concluded that the overall impact flash decay time primarily provides information regarding the physical nature of the target's surface, whereas the peak emission time is related to the properties of the impactor. This implies that the observed variation in peak intensity time in these two channels is likely linked to atomic/molecular emission involving aluminum. Figure 14 shows that one of the strongest emission

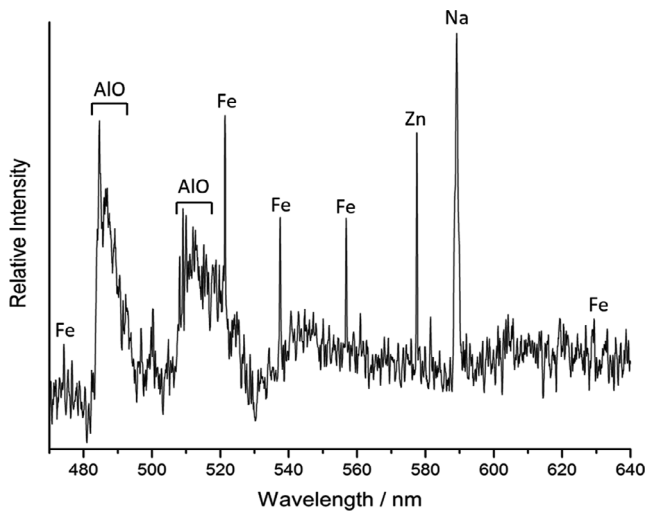


Fig. 14. Emission spectrum of a 3 mm 7075 Al projectile impacting a solid CO<sub>2</sub> ice target using a camera exposure time of 10  $\mu$ s. The spectrum comprises data from shots S7, S8, and S9 (468.7–530.9, 528.9–590.8, and 584.0–645.6 nm, respectively) with trigger delay times of 2.5, 1.4, and 2.1  $\mu$ s, respectively. Atomic/molecular assignments of the major emission lines/bands are indicated above. Observed Fe lines are most likely impurities originating from the stainless steel can.

bands in the observed spectrum is due to AIO between approximately 508 nm and 525 nm, coinciding with the spectral range of the photodiode channel centered at 513 nm. Additionally, the photodiode centered at 400 nm would capture the strong Al atomic emission lines at 394.4 and 396.2 nm. These Al/AIO emission lines/bands have been observed in previous impact experiments (Schultz 1996; Schultz et al. 1996; Heunoske et al. 2013; Tandy et al. 2014; Verreault et al. 2015) and all other Al atomic and AIO molecular emission would fall outside of the spectral regions covered by the remaining photodiodes. Yafei et al. (2019) also observed an earlier peak in the decay profile for the band-pass filtered photodiode centered at 400 nm, which would capture the aforementioned Al atomic emission.

Schultz (1996) first measured the impact-induced emission spectrum from a dry ice target and primarily observed AIO emission bands, from rapid impactor/target reactions within the ejecta cloud, and a strong Na atomic emission line at ~590 nm commonly observed from projectile impurity vaporization in impact experiments (e.g., Sugita et al. 2003; Tandy et al. 2014; Schultz and Eberhardy 2015). Figure 14 indicates that the same spectroscopic features are detected in this study, with strong AIO molecular emission between 484 and 525 nm (Pearse and Gaydon 1976) and a strong Na atomic line at 589.2 nm (Kramida et al. 2019). Additional atomic/molecular emission lines/bands

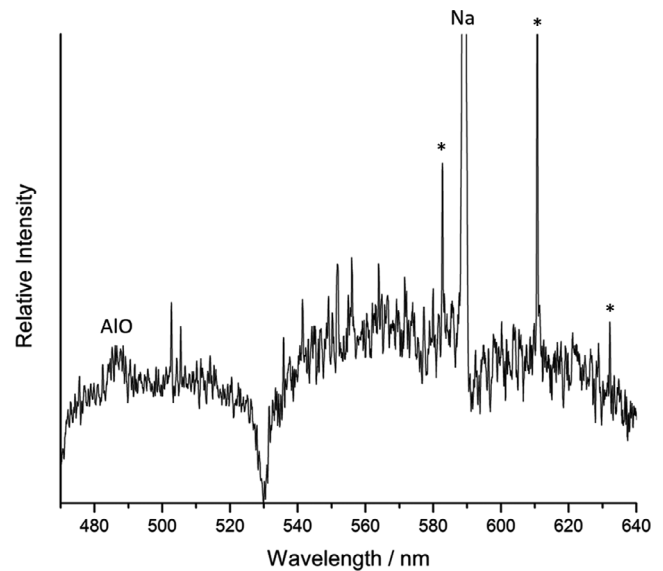


Fig. 15. Emission spectrum of a 3 mm diameter 7075 Al projectile impacting a solid 50% CO<sub>2</sub> ice/50% Martian regolith simulant using an exposure time of 10  $\mu$ s. The spectrum comprises data from shots S10, S11, and S12 (468.7–530.9, 528.9–590.8, and 584.0–645.6 nm, respectively) with trigger delay times of 7.2, 7.3, and 9.9  $\mu$ s, respectively. Atomic/molecular assignments of the major emission lines/bands are indicated above. The full intensity of the Na atomic emission line at ~590 nm is not shown to allow weaker emission lines/bands to be seen.

deriving from various sources are also observed. The Zn atomic emission line at ~578 nm originates from the projectile (7075 aluminum contains approximately 6% zinc), while multiple Fe lines are most likely impurities originating from the stainless steel can. Additional, weaker bands are also seen throughout the spectrum but cannot be conclusively assigned to specific atomic/molecular species.

One might expect CO bands from vaporized CO<sub>2</sub> ice target material to also be observed in emission. These bands have been previously detected in several other impact experiments using a variety of projectile and target materials (Schultz 1996; Schultz et al. 2007; Schultz and Eberhardy 2015). Three band heads of CO that are potentially evident within Fig. 14 are the 0–1, 0–2, and 0–3 ( $v' - v''$ )  $B^1 \Sigma - A^1 \Pi$  vibronic transitions, at 483.5, 519.8, and 561.0 nm, respectively (Pearse and Gaydon 1976). However, additional spectroscopic measurements for this projectile-target system would be required to conclusively assign these bands due to their very low intensities.

The significant difference in the spectral bands shown in Fig. 17 (corresponding to different vertical positions within the radiating plume) may explain slight inconsistencies in the emission spectra of shots S7–S9, where certain lines or bands may have been expected to

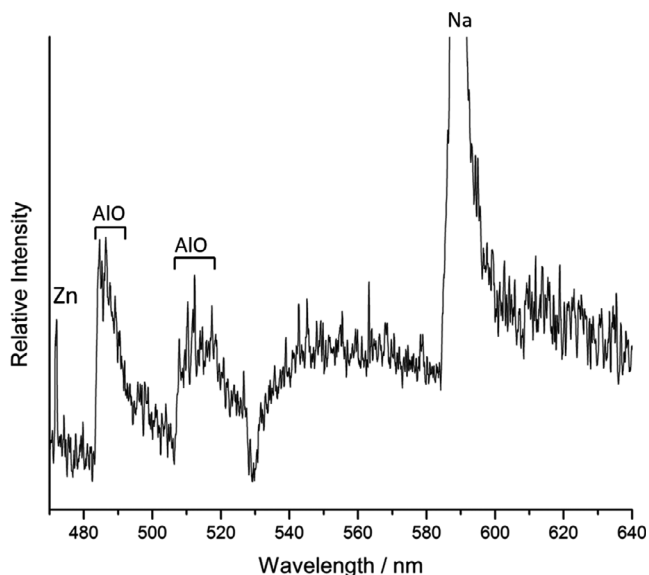


Fig. 16. Emission spectrum of a 3 mm diameter Al projectile impacting a solid 50% CO<sub>2</sub> ice/50% lunar regolith simulant using an exposure time of 10  $\mu$ s. The spectrum comprises data from shots S13, S14 (468.7–530.9, 528.9–590.8, and 584.0–645.6 nm, respectively), and S15 with trigger delay times of 4.5, 5.5, and 4.9  $\mu$ s, respectively. Atomic/molecular assignments of the major emission lines/bands are indicated above. The full intensity of the Na atomic emission line at ~590 nm is not shown to allow weaker emission lines/bands to be seen.

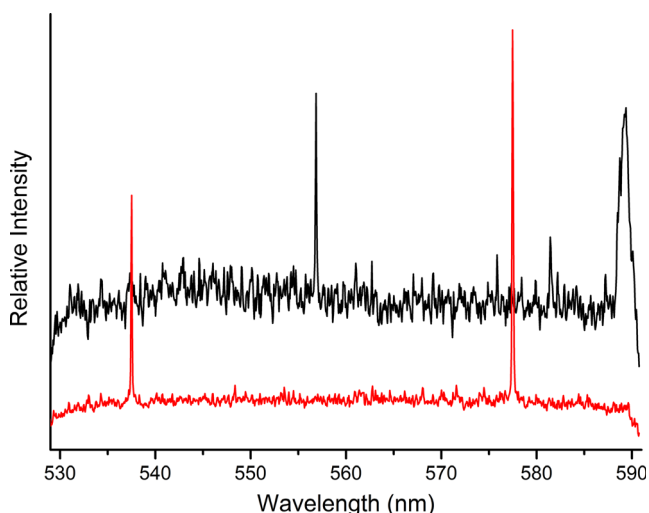


Fig. 17. Emission spectra of two data segments originating from shot S7 using a camera exposure time of 10  $\mu$ s with a trigger delay time of 1.4  $\mu$ s.

be more/less intense. For example, the relative intensity of the Fe lines observed in these spectra is not completely consistent with the Einstein coefficients for these transitions. Indeed, one might expect other strong

Fe lines (e.g., at ~532 nm) to be observed within the spectral region covered by Fig. 14 if the impact energy was evenly distributed throughout the radiating ejecta. The observed variation in emission within the ejecta may therefore provide an explanation for these slight inconsistencies. Sugita and Schultz (1999) also proposed that self-absorption of opaque, fine-grained debris/droplets may be responsible for inconsistent atomic emission intensities, which would likely exhibit strong blackbody radiation. Given the relatively low background shown in Fig. 17, it seems unlikely this is a primary cause of the observed intensity variations. Additionally, it is possible that the specific transitions measured in the current study provide a preferential decay pathway for the atomic/molecular species to dissipate their internal energy within the expanding ejecta cloud.

The mixed CO<sub>2</sub> ice and Martian regolith spectrum in Fig. 15 show a significant reduction in the AIO and Zn emission in comparison to the pure CO<sub>2</sub> ice target spectrum. Other weak emission features are also observed at approximately 582.7, 610.6, and 632.0 nm (indicated by an asterisk). These bands cannot be conclusively assigned, but approximately correspond to emission bands of FeO, CuO, and MgO, respectively (Pearse and Gaydon 1976), which could potentially originate from metal oxides within the Martian regolith, although these assignments are extremely tentative. Interestingly the, mixed CO<sub>2</sub> ice and lunar regolith spectrum in Fig. 16 shows a slight increase in AIO emission in comparison to Fig. 15, but shows no evidence of any bands corresponding to metal oxide emission.

The reduced projectile emission observed in Figs. 15 and 16 correlates with an increase in trigger delay time of the spectrometer, with the lowest AIO emission for the Martian regolith-containing target corresponding to the largest average trigger delay. This observation is consistent with the most intense projectile emission occurring during the short-lived jetting phase immediately after impact (Sugita and Schultz 1999; Schultz and Eberhardy 2015). The apparent disappearance of the bands potentially corresponding to FeO, CuO, and MgO in Fig. 16 might be explained by the reduction in metal oxide composition (except for CaO) within the lunar regolith simulant (Appendix A).

The relative proportion of emission lines/bands originating from the projectile and target materials at different stages after impact has been previously investigated (Sugita and Schultz 1999; Schultz and Eberhardy 2015). Schultz and Eberhardy (2015) concluded that, at distances relatively close to the point of impact, early-time emission spectra (within the first 20  $\mu$ s after impact) are dominated by projectile emission

caused by high-speed jetting. Given the short exposure time and positioning of the spectrometer system, the strongest lines/bands within emission spectra of this study should therefore originate from the projectile, which is confirmed by the relative intensities in Fig. 14. Sugita et al. (2003, 2004) showed the relative intensity of such optical emission is strongly controlled by the partition function and the degrees of electronic excitation and ionization. Furthermore, the specific electronic excitation energies were shown to govern the relative intensities between emission lines from identical elements and the degree of ionization shown to primarily control the intensity ratio of emission lines between different atomic species. The apparent lack of clear spectral signatures other than AIO indicates that the majority of the emitting species within the self-luminous plume originate from the aluminum projectile, with little or no contribution from vaporized species from the target material. This may be due to insufficient energy from the relatively small-scale impact to ionize or electronically excite the necessary quantity of target material. The spectra also show little evidence of an underlying high temperature, blackbody background, suggesting that the detected ejecta/condensates (originating from the vapor plume) are relatively cool. This is expected given the position of the spectrometer, which would allow considerable expansion and cooling of this material before entering the specific field of view of the PI-MAX4 camera (Fig. 4).

Figure 7 illustrates the considerable differences in the relative peak emission for the various target materials within each photodiode channel. Despite these deviations, a few general conclusions can be made (when using aluminum projectiles):

1. The average peak emission intensity of the 100% water ice is considerably lower than the other targets.
2. The average peak emission intensity is higher when using CO<sub>2</sub> ice (rather than water ice) within the target.
3. The average peak emission intensity is higher for targets containing the lunar regolith simulant in comparison to the Martian regolith simulant.
4. The primary emission peak occurs slightly later for targets containing lunar or Martian regolith simulant.

The FastCan camera photographs in Appendix B (recorded for shots S1, S2, S5, and S6) also confirm the general trend that targets containing CO<sub>2</sub> ice yield brighter impact flashes in comparison to those that contain water ice.

These trends may potentially be explained by the relative densities of the different target materials: the measured densities for the water-containing targets show an increase in density from pure water ice to

frozen Martian regolith to frozen lunar regolith, and CO<sub>2</sub> ice has a higher density (between 1.4 and 1.6 g cm<sup>-3</sup> from Häring et al. 2007) than water ice. The delayed emission peak of the regolith-containing targets could also be explained by the increased obscuration caused by the ejecta from these materials. A higher proportion of the pure ice targets (water or CO<sub>2</sub>) will be vaporized upon impact, meaning a reduction in the solid debris obscuring the initial flash. Ejecta from regolith-containing targets would therefore need to expand further before the maximum emission intensity could be detected by the photodiode array.

The range of decay exponent ( $\alpha$ ) values shown in Fig. 8 reflects the considerable variation in the properties of the six target materials and correlates well with the general trends observed for the peak emission intensities:

1. The relative rate of decay of the 100% water ice emission is considerably longer than the other targets.
2. The relative rate of decay is shorter when using CO<sub>2</sub> ice (rather than water ice) within the target.
3. The relative rate of decay is shorter for targets containing the lunar regolith simulant in comparison to the Martian regolith simulant.

The  $\alpha$  values of the mixed water ice and lunar/Martian regolith simulant targets also compare favorably with the decay exponent obtained by Ernst and Schultz (2003) for a frozen perlite target ( $\alpha = -1.02$ ).

Figure 9 shows a strong, linear correlation between the decay exponent and target density (for water ice-containing targets), with  $\alpha$  decreasing for increasing target density, as previously noted by Ernst and Schultz (2003) for sand, pumice, and perlite targets. Their examination of frozen and unfrozen perlite targets also showed a greater excavation efficiency in particulate targets, corresponding to a smaller  $\alpha$  (longer rate of decay) for the unfrozen sample. The Martian regolith-containing targets of this work were observed to break apart much more easily during preparation, with the mixed CO<sub>2</sub> ice and Martian regolith targets requiring slightly more water to effectively bind the materials. The greater particulate nature of the Martian regolith-containing targets (in comparison to the lunar regolith) is likely related to the larger average grain size and is also reflected in the considerably smaller  $\alpha$  values shown in Fig. 8. A future study examining the correlation between grain size distribution and decay exponent is therefore warranted to ascertain the importance of this parameter in the emission decay for various target materials.

Despite the strong correlation between decay exponent and target density observed, several factors

are known to contribute to the impact flash decay. First, the porosity of the target has been shown to significantly alter the emission decay and duration (Ernst and Schultz 2003, 2007; Schultz et al. 2005) with highly porous particulate targets reducing the flash lifetime by more than two orders of magnitude. Although it is difficult to assess the exact porosity of the frozen, mixed ice, and regolith targets, the average grain size for the Martian regolith simulant used in this study was considerably larger than the lunar simulant, which may correlate to a decreased porosity within the frozen targets. This would imply a slower emission decay in the Martian regolith-containing targets in comparison to those containing lunar regolith, which is supported by the alpha values shown in Fig. 8. However, the precise correlation between grain size and porosity upon impact for frozen targets has not been established meaning a clear correlation between porosity and decay exponent cannot be determined for the target materials used in this study. Indeed, the simulants used do not reflect the true grain size distribution for either Martian or lunar regolith, but were utilized for their chemical similarity. It is also likely that the relative composition of the mixed ice regolith targets would affect this parameter and should be investigated further to examine a possible correlation between decay exponent and the percentage of regolith used within the frozen target. Second, the difference between solid and particulate targets has been shown to reduce peak emission duration by a factor of two (Ernst and Schultz 2007). Given that all targets within this study were frozen into a solid block, it seems likely that this parameter should not have significantly affected the measured decay exponents.

Third, the volatile content of the target is also understood to influence the blackbody radiation that contributes toward the impact flash lifetime (Ernst and Schultz 2003; Schultz et al. 2005). An increased volatile content generally yields a greater radiant energy for a volatile-rich projectile–target system like Al onto CO<sub>2</sub> ice. This manifests itself in the more intense AlO emission bands from the pure CO<sub>2</sub> ice target (Fig. 14) in comparison to the mixed regolith-ice target spectra (Figs. 15 and 16). If volatile content were the major factor in the determination of the decay exponent, one would expect the  $\alpha$  value for the pure CO<sub>2</sub> ice to be smaller (i.e., longer decay time) than the equivalent values for the two mixed CO<sub>2</sub>-regolith targets, as the overall heat of vaporization/sublimation for regolith-containing targets should be considerably larger. Figure 8 illustrates that this is not the case with the pure CO<sub>2</sub> ice  $\alpha$  value (−1.751) greater than the mixed CO<sub>2</sub> ice and Martian regolith value (−1.347), but less than mixed CO<sub>2</sub> ice and lunar regolith value (−2.434).

However, the observed pure water ice  $\alpha$  value (−0.196) is considerably smaller than both the mixed water ice and regolith decay exponents (Martian = −0.904 and lunar = −1.650) despite the intensity of the emission for water ice being considerably weaker (Fig. 7). Additionally, the  $\alpha$  values for the CO<sub>2</sub> ice-containing targets are all lower than the equivalent values for the water ice-containing targets, which fit an increased CO<sub>2</sub> vapor content within the ejecta plume in comparison to water vapor when using the same impact parameters. These observations suggest that an increased content of vaporized material may cause a slower decay in emission, but is likely one of several contributing factors as previously shown by Eberhardy, Ernst, and Schultz (Ernst and Schultz 2003, 2007; Schultz et al. 2005; Schultz and Eberhardy 2015).

The decay exponents and best-fit equation of Fig. 9 were subsequently used to estimate densities for the CO<sub>2</sub> ice-containing target materials of 1.61, 1.39, and 1.99 g cm<sup>−3</sup> for the 100% CO<sub>2</sub> ice, 50% CO<sub>2</sub> ice/50% Martian regolith, and 50% CO<sub>2</sub> ice/50% lunar regolith targets, respectively, with a relative standard deviation of 2.8% (determined from the  $R^2$  value of Fig. 9). The density value determined for the 100% CO<sub>2</sub> ice target is in good agreement with the typical density of dry ice at room temperature (~1.5 g cm<sup>−3</sup>, Häring et al. 2007) suggesting that the method is relatively precise and could potentially be a useful tool to determine the composition of an unknown target material. However, considerable further investigation would be required to determine the applicability of this method for different target materials given the other contributing factors discussed above.

Additional variations were also observed in the shape of the decay profiles (Fig. 7), with certain photodiode channels showing secondary peaks at times greater than 0.8 ms after impact. Indeed, three decay profiles (two in the 355 nm channel and one in the 905 nm channel) show secondary peaks with a larger emission intensity than the initial peak. Initially, one might think that these later emission peaks (generally between 0.8 and 1.8 ms) provide evidence of a secondary impact onto the target. If this was the case, a secondary peak should occur at approximately the same time within all photodiode channels and Fig. 7 illustrates that this is not observed. Furthermore, no additional impactors (>50 microns in size—the lower detection limit) were detected by the time-of-flight system during any of these shots. The spectral variations shown in Fig. 17 also suggest that the composition of the ejecta within the first few microseconds after impact is inhomogeneous with radiating atomic/molecular species localized to specific areas. Indeed, Schultz and Eberhardy (2015) successfully measured differences in emission spectra resulting from

multiple components of the ejecta/condensates passing through the field of view of their spectrometer system while tracking the ejecta's evolution.

One possible explanation for these secondary peaks would be due to reflected vapor phase emission from ejecta/debris that have impacted the target chamber walls. Given the shortest distance from the target to the chamber wall, a minimum ejecta/debris velocity of approximately  $2 \text{ km s}^{-1}$  would be required to produce the secondary emission at  $\sim 1 \text{ ms}$  in the observed photodiode decay profiles. This velocity is certainly achievable given the rapidly expanding ejecta/condensate emission shown in Fig. 6. The diverse range of speeds and trajectories of the reflected luminous parcels may also explain the varied timings of secondary peaks in different photodiode channels. However, it is not currently clear whether such contributions from reflected ejecta/debris would be sufficiently bright to cause observable secondary peaks within the first few milliseconds after impact.

Another potential explanation for the additional peaks could be the presence of "pockets" of emitting material embedded within the more dense ejecta. These "pockets" would be initially obscured from the field of view of each photodiode, but would become visible as the ejecta expands into the target chamber. This explanation is supported by the previously discussed segmented emission spectra, which suggests an inhomogeneous composition of the observed ejecta. This is also supported by the high-speed images of Schultz et al. (2007) that show small pieces of self-luminous impact melt that emerge from the growing impact crater cavity after the initial impact flash.

A third explanation is that the emission is actually generated during the expansion of the ejecta. This could potentially occur from physical and/or chemical processes within the ejecta creating emitting atomic or molecular species, or from a secondary reflected shock produced from the interface between target material and steel can. Interestingly, the secondary peaks were only observed for targets containing lunar or Martian regolith simulant, suggesting that the target composition may be critical to their occurrence. A more detailed spectroscopic study would be required to clearly understand the wavelength dependence of these secondary emission peaks and conclusively determine their origin.

Impact speed has also been shown to significantly affect the behavior of ejecta emission. Sugita et al. (2003) observed a strong dependence on impact speed for the total intensity of optical emission between 435 and 650 nm for copper impacts onto dolomite targets and showed that the flash intensity was approximately proportional to the fifth power of impact speed, between 2 and  $5.5 \text{ km s}^{-1}$ . Previous studies by Eichhorn

(1975, 1976) also showed a strong correlation between emission rise time and impact speed for iron and aluminum impacts onto tungsten and gold targets using a Van der Graff accelerator. Figure 13 indicates a similar trend for emission decay rate with a strong, linear correlation between the impact speed and decay exponent for  $\text{CO}_2$  ice targets, with  $\alpha$  decreasing for increasing impact speed. This observation warrants considerable further investigation to determine if similar trends are also observed for different target materials. However, additional information can be ascertained by examining the change in emission profile with increasing impact speed.

Interestingly, the  $5.73 \text{ km s}^{-1}$  profile in Fig. 12 strongly resembles that of a previously observed flash decay from a  $30^\circ$ ,  $5.7 \text{ km s}^{-1}$  impact into sugar using a 0.64 cm Pyrex sphere (Ernst and Schultz 2007). Figures 10–12 clearly indicate the three-component behavior of the impact flash reported by Bergeron et al. (2006), Lawrence et al. (2006), and Ernst et al. (2011). These components consist of (1) an early-time spike, (2) a generally broader peak, and (3) a longer decaying signal. Previous studies have shown that the second of these components typically dominates the emission signal (Ernst and Schultz 2004; Ernst et al. 2011; Yafei et al. 2019). However, Figs. 10–12 indicate that this may not be the case at lower velocities, with the flash decaying immediately after the initial spike for the impact at  $4.03 \text{ km s}^{-1}$ .

Ernst et al. (2011) previously reported an increase in intensity of the initial spike with increasing impact speed for oblique impacts. They concluded that changes to this component correlate to an alteration in the interaction duration between projectile and target. Lower impact speeds allow a longer interaction, while higher impact velocities break up the projectile more efficiently into emitting fragments. The data shown in Figs. 10–12 are consistent with this explanation, with the initial component becoming more prevalent at higher impact speeds. These figures also indicate that the changes in intensity of this component are wavelength independent.

Additionally, Figs. 10–12 suggest that higher impact speeds, corresponding to a greater impact energy, maintain the duration of the initial spike, but delay the peak emission intensity of the second component. The magnitude of this delay is also shown to be wavelength dependent, with the 513 nm photodiode channel exhibiting a comparatively reduced extension in the maximum intensity of the second component as impact speed increases. As previously discussed, this channel corresponds to the spectral region of strongest molecular emission, which appears to alter the behavior of the decay profile. In the majority of photodiode channels, the temporal behavior of the second component is



primarily determined by the expansion time of the radiating ejecta cloud: the emission intensity increases to a peak as more radiating fragments are visible to the photodiode array. The signal in the 513 nm channel peaks and decays more quickly, which is consistent with a signal dominated by AIO molecular emission. The reduced extension in peak intensity for the second component indicates that AIO emission does not significantly increase as the ejecta cloud expands, which is consistent with the short lifetime of optical molecular emission and projectile-containing species primarily forming and emitting during the initial jetting phase.

At higher velocities relatively more radiating material is excavated from the target, meaning a lower proportion of emitting ejecta will correspond to the atomic/molecular emission from projectile-containing species. This implies that at a sufficiently high velocity, the AIO molecular emission would no longer dominate the second component of the 513 nm channel and would appear more similar to decay profiles at other wavelengths. Additionally, this suggests that band-pass filters must be sufficiently narrow and centered at a wavelength corresponding to a peak in atomic/molecular emission in order to detect similar behavior. It is also worth noting that the impact flash is also highly dependent on the angle of impact (Schultz 1996; Schultz et al. 1996; Sugita and Schultz 1999; Yafei et al. 2019), and will likely alter the decay profile for impacts into frozen targets.

## CONCLUSIONS

This study illustrates the considerable benefits of spectroscopically examining impact ejecta, which show a strong and varied wavelength dependence on several impact parameters, with atomic/molecular emission influencing the temporal evolution of the ejecta flash. Future investigation of this wavelength dependence utilizing a fully calibrated photodiode array may yield more reliable absolute detector intensities, which could be used to determine the temporal evolution of the ejecta temperature. Emission spectra from Al impacts into CO<sub>2</sub> ice and simulant-based targets show consistent contributions from AIO originating from the projectile. There appears to be very little or no emission that originates solely from the target material (e.g., CO emission), perhaps due to insufficient energy from the relatively small-scale impact. Despite this, these observations may provide a useful comparison for future observations of impact flashes on the Moon, Mars, and other frozen planetary bodies with a high surface composition of water or CO<sub>2</sub> ice.

The occurrence of multiple peaks within the impact flash decay profiles and differences in the segmented

emission spectra indicates an inhomogeneous ejecta composition, as previously identified by Schultz and Eberhardy (2015) for impacts into powdered dolomite targets. A future comparison of flash decay profiles and emission spectra at different ejecta trajectories may therefore provide additional information regarding potential compositional changes at different locations around a crater site and determine a broader range of emitting atomic/molecular species present within the ejecta plume. The apparent strong correlation between target density and the rate of decay of the impact flash (in spectral regions without significant atomic/molecular emission) warrants further investigation using varied projectile and target materials. Such studies may assist in the determination of an underlying cause and potentially allow subsequent analyses to determine approximate densities of an unknown target material.

Changes in the initial flash intensity due to an increase in impact speed were shown to be wavelength independent. A strong, linear correlation is also shown between impact speed and decay exponent for CO<sub>2</sub> ice targets. Additionally, an increase in impact speed appears to maintain the duration of the flash's initial, short-lived peak, but alters the temporal behavior of the secondary rise in emission intensity and its subsequent decay. These features also show a wavelength dependence, indicating further influence from strong atomic/molecular emission. These observations highlight the importance of using a wide range of impact parameters in both laboratory experiments and modeling when investigating complex ejecta phenomena.

*Acknowledgments*—The authors thank Prof. Peter Schultz and an anonymous reviewer for their helpful comments. We thank Dr Phillipa Timmins and Princeton Instruments for the loan of the high-speed spectrometer system. MCP, MJC, and JT thank the STFC for help in funding this work. JT thanks Wiktoria Fiolek and Yasin Malik for their assistance with the density measurements of the frozen targets. LA acknowledges receipt of a University of Kent GTA Scholarship. CA thanks ESA Science Faculty grant for building the detection instrument. The work of CA was supported by the French National Research Agency under the project “Investissements d’Avenir” UCAJEDI with the reference number ANR-15-IDEX-01. The program “Flash!” of CA was supported by the Programme National de Planetologie (PNP) of CNRS/INSU, co-funded by CNES, and by the Crédits Scientifiques Incitatifs (CSI) of the Université Nice Sophia Antipolis.

*Editorial Handling*—Dr. Gordon Osinski.

## REFERENCES

- Allen C. C., Jager K. M., Morris R. V., Lindstrom D. J., Lindstrom M. M., and Lockwood J. P. 1998. Martian soil simulant available for scientific, educational study. *Earth and Space Science News* 79:405–409.
- Ang J. A. 1990. Impact flash jet initiation phenomenology. *International Journal of Impact Engineering* 10:23–33.
- Avdellidou C. and Vaubaillon J. 2019. Temperatures of lunar impact flashes: Mass and size distribution of small impactors hitting the Moon. *Monthly Notices of the Royal Astronomical Society* 484:5212–5222.
- Avdellidou C., Price M. C., Delbo M., and Cole M. J. 2017. Survival of the impactor during hypervelocity collisions—II. An analogue for high-porosity targets. *Monthly Notices of the Royal Astronomical Society* 464:734–738.
- Bergeron N. P., Hollerman W. A., Goedeke S. M., Hovater M., Hubbs W., Finchum A., Moore R. J., Allison S. W., and Edwards D. L. 2006. Experimental evidence of triboluminescence induced by hypervelocity impact. *International Journal of Impact Engineering* 33:91–99.
- Bruck Syal M., Schultz P. H., and Crawford D. A. 2012. Impacts into porous and nonporous ice targets. Abstract 202–11. Charleston, North Carolina: Geological Society of America.
- Burchell M. J., Cole M. J., and Ratcliff P. R. 1996. Light flash and ionization from hypervelocity impacts on ice. *Icarus* 122:359–365.
- Burchell M. J., Cole M. J., McDonnell J. A. M., and Zarnecki J. C. 1999. Hypervelocity impact studies using the 2 MV Van de Graaff dust accelerator and two stage light gas gun of the University of Kent at Canterbury. *Measurement Science & Technology* 10:41–50.
- Cudnik B. M., Dunham D. W., Palmer D. M., Cook A., Venable R., and Gural P. S. 2003. Ground-based observations of lunar meteoritic phenomena. *Earth, Moon, and Planets* 93:145–161.
- Dunham D. W., Cudnik B., Palmer D. M., Sada P. V., Melosh J., Frankenberger M., Beech R., Pellerin L., Venable R., Asher D., Sterner R., Gotwols B., Wun B., and Stockbauer D. 2000. The first confirmed video recordings of lunar meteor impacts (abstract #1547). 31st Lunar and Planetary Science Conference. CD-ROM.
- Eichhorn G. 1975. Measurements of the light flash produced by high velocity particle impact. *Planetary and Space Science* 23:1519–1525.
- Eichhorn G. 1976. Analysis of the hypervelocity impact process from impact flash measurements. *Planetary and Space Science* 24:771–781.
- Ernst C. M. and Schultz P. H. 2003. Effect of initial conditions on impact flash decay (abstract #2020). 34th Lunar and Planetary Science Conference. CD-ROM.
- Ernst C. M. and Schultz P. H. 2004 (abstract #1721). 35th Early-time temperature of the impact flash and beyond 2004. Lunar and Planetary Science Conference. CD-ROM.
- Ernst C. M. and Schultz P. H. 2007. Evolution of the Deep Impact flash: Implications for the nucleus surface based on laboratory experiments. *Icarus* 190:334–344.
- Ernst C. M., Barnouin O. S., and Schultz P. H. 2011. Comparing experimental and numerical studies of the impact flash: Implications for impact melt generation. *EPSC Abstracts, EPSC-DPS Joint Meeting* 2011:1484.
- Gehring J. W. and Warnica R. L. 1963. An investigation of the phenomena of impact flash and its potential use as a hit detection and target discrimination technique. *Proceedings of the Sixth Symposium on Hypervelocity Impact* 2:627–682.
- Goel A., Lee N., and Close S. 2015. Estimation of hypervelocity impact parameters from measurements of optical flash. *International Journal of Impact Engineering* 84:54–63.
- Häring H.-W., Ahner C., and Belloni A. 2007. *Industrial gases processing*. Weinheim: Wiley-VCH.
- Heunoske D., Schimmerohn M., Osterholz J., and Schafer F. 2013. Time-resolved emission spectroscopy of impact plasma. *Procedia Engineering* 58:624–633.
- Jean B. and Rollins T. L. 1970. Radiation from hypervelocity impact generated plasma. *The American Institute of Aeronautics and Astronautics* 8:1742–1748.
- Kadono T. and Fujiwara A. 1996. Observation of expanding vapor cloud generated by hypervelocity impact. *Journal of Geophysical Research* 101:26,097–26,109.
- Kondo K. and Ahrens T. J. 1983. Heterogeneous shock-induced thermal radiation in minerals. *Physics and Chemistry of Minerals* 9:173–181.
- Kramida A., Ralchenko Y., Reader J., and NIST ASD Team. 2019. *NIST Atomic Spectra Database* (ver. 5.7.1). Gaithersburg, Maryland: National Institute of Standards and Technology. <https://doi.org/10.18434/T4W30F>.
- Lawrence R. J., Reinhart W. D., Chhabildas L. C., and Thornhill T. F. 2006. Spectral measurements of hypervelocity impact flash. *International Journal of Impact Engineering* 33:353–363.
- Martins Z., Price M. C., Goldman N., Sephton M. A., and Burchell M. J. 2013. Shock synthesis of amino acids from impacting cometary and icy planet surface analogues. *Nature Geoscience* 6:1045–1049.
- McKay D. S., Carter J. L., Boles W. W., Allen C. C., and Allton J. H. 1994. JSC-1: A new lunar soil simulant. *Proceedings from International Symposium on Engineering, Construction and Operations in Space IV*. Reston, Virginia: ASCE. pp. 857–866.
- Mihaly J. M., Tandy J. D., Adams M. A., and Rosakis A. J. 2013. In situ diagnostics for a small-bore hypervelocity impact facility. *International Journal of Impact Engineering* 62:13–26.
- Mihaly J. M., Tandy J. D., Rosakis A. J., Adams M. A., and Pullin D. 2015. Pressure-dependent, infrared-emitting phenomenon in hypervelocity impact. *Journal of Applied Mechanics* 82:011004.
- Pearse R. W. B. and Gaydon A. G. 1976. *The identification of molecular spectra*, 4th ed. New York: Chapman and Hall.
- Pospieszalska M. K. and Johnson R. E. 1991. Micrometeorite erosion of the main rings as a source of plasma in the inner saturnian plasma torus. *Icarus* 93:45–52.
- Rager A. H., Smith E., Scheu B., and Dingwell D. B. 2014. The effects of water vaporization on rock fragmentation during rapid decompression: Implications for the formation of fluidized ejecta on Mars. *Earth and Planetary Science Letters* 385:68–78.
- Schultz P. H. 1996. Effect of impact angle on vaporization. *Journal of Geophysical Research* 101:21,117–21,136.
- Schultz P. H. and Eberhardy C. A. 2015. Spectral probing of impact-generated vapor in laboratory experiments. *Icarus* 248:448–462.
- Schultz P. H. and Mustard J. F. 2004. Impact melts and glasses on Mars. *Journal of Geophysical Research* 109: E01001.

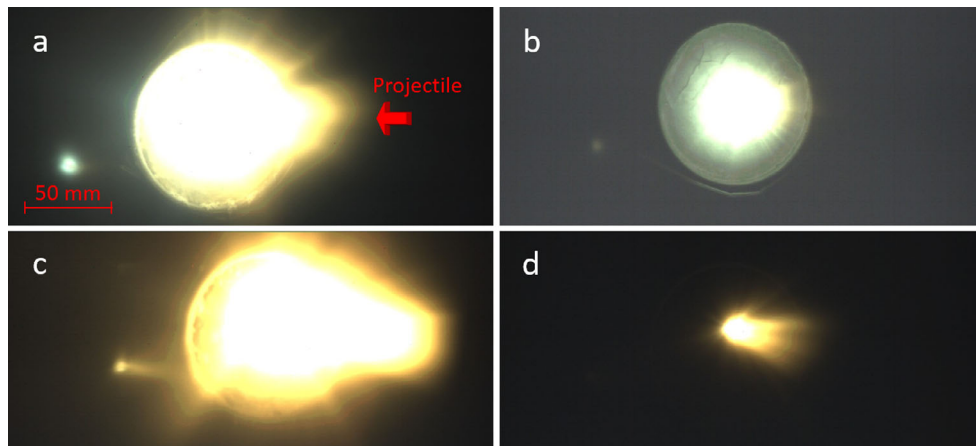
- Schultz P. H., Adams M. A., Perry J. W., Goguen J. D., and Sugita S. 1996. Impact flash spectroscopy. *Proceedings, 27th Lunar and Planetary Science Conference*. pp. 1149–1150.
- Schultz P. H., Ernst C. M., and Anderson J. L. B. 2005. Expectations for crater size and photometric evolution from the deep impact collision. *Space Science Reviews* 117:207–239.
- Schultz P. H., Sugita S., Eberhardy C. A., and Ernst C. M. 2006. The role of ricochet on impact vaporization. *International Journal of Impact Engineering* 33:771–780.
- Schultz P. H., Eberhardy C. A., Ernst C. M., A’Hearn M. F., Sunshine J. M., and Lisse C. M. 2007. The deep impact oblique impact cratering experiment. *Icarus* 191:84–122.
- Suggs R. M., Moser D. E., Cooke W. J., and Suggs R. J. 2014. The flux of kilogram-sized meteoroids from lunar impact monitoring. *Icarus* 238:23–36.
- Sugita S. and Schultz P. H. 1999. Spectroscopic characterization of hypervelocity jetting: Comparison with a standard theory. *Journal of Geophysical Research* 104:30825–30845.
- Sugita S. and Schultz P. H. 2003a. Interactions between impact-induced vapor clouds and the ambient atmosphere: 1. Spectroscopic observations using diatomic molecular emission. *Journal of Geophysical Research* 108:5051.
- Sugita S. and Schultz P. H. 2003b. Interactions between impact-induced vapor clouds and the ambient atmosphere: 2. Theoretical modelling. *Journal of Geophysical Research* 108:5052.
- Sugita S., Schultz P. H., and Adams M. A. 1998. Spectroscopic measurement of vapor clouds due to oblique impacts. *Journal of Geophysical Research* 103:19,427–19,441.
- Sugita S., Schultz P. H., and Hasegawa S. 2003. Intensities of atomic and molecular bands observed in impact-induced luminescence. *Journal of Geophysical Research* 108:5140.
- Sugita S., Schultz P. H., and Hasegawa S. 2004. What controls the intensity of impact-induced luminescence? (abstract #1048). 35th Lunar and Planetary Science Conference. CD-ROM.
- Tandy J. D., Mihaly J. M., Adams M. A., and Rosakis A. J. 2014. Examining the temporal evolution of hypervelocity impact phenomena via high-speed imaging and ultraviolet-visible emission spectroscopy. *Journal of Applied Physics* 116:034901.
- Timmermann R. and Grün E. 1991. Plasma emission from high velocity impacts of microparticles onto water ice. In *Origin and evolution of interplanetary dust*, edited by Levasseur-Regourd A. C. and Hasegawa H. *Proceedings, 126th Colloquium of the International Astronomical Union* 173:375–378.
- Tsembelis K., Burchell M. J., Cole M. J., and Margaritis N. 2008. Residual temperature measurements of light flash under hypervelocity impact. *International Journal of Impact Engineering* 35:1368–1373.
- Verreault J., Day J. P. R., Halswijk W. H. C., Loiseau J., Huneault J., Higgins A. J., and Devir A. D. 2015. Emission spectroscopy of hypervelocity impacts on aluminum, organic and high-explosive targets. *Procedia Engineering* 103:618–627.
- Yafei H., Enling T., Liping H., Meng W., Kai G., Jin X., Jianjun M., Shuhua L., Ruizhi W., and Zhenbo L. 2019. Evolutionary characteristics of thermal radiation induced by 2A12 aluminum plate under hypervelocity impact loading. *International Journal of Impact Engineering* 125:173–179.
- Yang W., Ahrens T. J., Miller G. H., and Petach M. B. 1992. Jet ejecta mass upon oblique impact. In *Shock compression of condensed matter*, edited by Schmidt S. C., Dick R. D., Forbes J. W. and Tasker D. G. New York: North Holland. pp. 1011–1014.

## APPENDIX A

Chemical composition of JSC-1A lunar (McKay et al. 1994) and JSC-1 Martian (Allen et al. 1998) regolith simulants.

Component	JSC-1A Lunar simulant % weight	JSC-1 Martian simulant % weight
SiO <sub>2</sub>	47.7	43.5
Al <sub>2</sub> O <sub>3</sub>	15.0	23.3
TiO <sub>2</sub>	1.6	3.8
Fe <sub>2</sub> O <sub>3</sub>	3.4	15.6
MnO	–	0.3
CaO	10.4	6.2
K <sub>2</sub> O	–	0.6
Na <sub>2</sub> O	2.7	2.4
P <sub>2</sub> O <sub>5</sub>	–	0.9

## APPENDIX B B



Impact flash photographs recorded from a 3 mm diameter Al projectile impacting solid targets of (a) CO<sub>2</sub> ice, (b) water ice, (c) 50% CO<sub>2</sub> ice/50% JSC-1A lunar regolith simulant, and (d) 50% water ice/50% JSC-1A lunar regolith simulant, corresponding to shots S1, S2, S5, and S6, respectively. The frame with greatest emission intensity for each target material was selected for comparison. Each photograph has an exposure time of approximately 0.35 ms, although exact timings of each frame relative to the impact time could not be determined. The bright area on the left side of images (a), (b), and (c) are due to specular reflection from the steel can containing the frozen target. The edge of the steel can is also observed as the circular feature in these images.